

TECHNICAL NOTE

Glovebox-integrated XES and XAS station for *in situ* studies in tender x-ray region

To cite this article: Mohsen Shakouri *et al* 2020 *Electron. Struct.* **2** 047001

View the [article online](#) for updates and enhancements.



The Electrochemical Society
Advancing solid state & electrochemical science & technology



239th ECS Meeting with IMCS18
ECS PLENARY LECTURE - **CARBON MATERIALS**
Presenter: **Rodney S. Ruoff**, Ulsan National Institute of Science & Technology

DIGITAL EVENT • May 31, 2021, 2100-2200 EDT • No cost to attend



REGISTER NOW

Electronic Structure



TECHNICAL NOTE


Glovebox-integrated XES and XAS station for *in situ* studies in tender x-ray region

RECEIVED
23 June 2020

REVISED
28 August 2020

ACCEPTED FOR PUBLICATION
16 September 2020

PUBLISHED
6 October 2020

Mohsen Shakouri¹ , William M Holden², Yongfeng Hu^{1,*}, Qunfeng Xiao¹,
Ru Igarashi¹, Bryan Schreiner¹, Michael Bree¹, Minsi Li^{3,4}, Weihai Li^{3,4}, Xueliang Sun³
and Tsun-Kong Sham⁴

¹ Canadian Light Source, 44 Innovation Boulevard, Saskatoon, Saskatchewan, S7N 2V3, Canada

² easyXAFS LLC, Renton, Washington 98057, United States of America

³ Department of Mechanical and Materials Engineering, University of Western Ontario, London, Ontario, N6A 5B9, Canada

⁴ Department of Chemistry and Soochow-Western Centre for Synchrotron Radiation Research, University of Western Ontario, London, Ontario, N6A 5B7, Canada

* Author to whom any correspondence should be addressed.

E-mail: Yongfeng.Hu@lightsource.ca

Keywords: x-ray spectroscopy, tender x-ray, XES, *in situ*, lithium-ion battery

Abstract

X-ray emission spectroscopy (XES), as a complementary technique to x-ray absorption spectroscopy (XAS), is powerful in the analysis of the electronic structure of the materials by probing the occupied density of states with high energy resolution. Recently, an XES spectrometer optimized for the tender x-ray region (2–5 keV) was successfully installed into an inert atmosphere glovebox, and the entire system was successfully integrated into the SXRMB (soft x-ray microcharacterization beamline) at the Canadian Light Source. Here, the technical design and the performance of the SXRMB XES-integrated glovebox station is presented. High energy resolution of ~ 1 eV or better has been achieved for the spectrometer in the tender energy x-ray ranges. Capability of the station for *in-situ* XES and XAS measurements is demonstrated using an example of phosphorus phase transformation in phosphorus anodes for lithium-ion battery research.

1. Introduction

Chemical analysis, structural parameters and electronic properties of materials are essential for many fundamental studies and industrial applications. Understanding the local geometry, charge density and type of ligands attached to the element of interest in materials is key for studies in materials science, chemistry, catalysis, medicine, earth and environmental sciences [1–6]. In addition, probing the chemical structure of materials under actual working conditions is necessary in material development, catalysis and energy device studies [7–9]. Several synchrotron-based, and more recently benchtop laboratory-scale, spectroscopy and microscopy techniques have been used to address these questions. Synchrotron-based techniques are more powerful for various reasons such as the tunability, brilliance, flux, and better detection limits with the synchrotron x-ray sources [4]. Among them, x-ray absorption spectroscopy (XAS) is more developed and widely used technique to obtain information about the electronic properties and coordination information such as types and number of neighbouring atoms of the centre atom. Though, when the neighbouring atoms have close atomic numbers (e.g., when a central metal atom bonds to N, O, and C), XAS should be coupled with other spectroscopic techniques to provide detailed understanding. X-ray emission spectroscopy (XES) can be used complementary to XAS. While the XAS probes transitions of a core hole electron to empty states above the Fermi level, XES can be used as a measure to probe the filled electron orbitals and obtain information on the charge density [4, 10]. Thus, XES can give more direct information in ligand identification especially in ligands with similar atomic numbers.

Up to now, there have been limited synchrotron-based XES endstations at beamlines, including SuperXAS beamline at the SLS [11], ID-26 beamline at the ESRF [12], BM30B/CRG-FAME XAS [13] and Rossendorf beamlines at the ESRF [14], beamline 6-2 at the SSRL [15, 16] and beamline P 64 at the PETRA III [17]. Most

of these endstations are designed mainly for hard x-ray (>5 keV) applications, where it is relatively straightforward to set up the XES spectrometer and measurement in ambient environment. Comparatively, there are few XES endstations for elements in the medium/tender energy range (between 1 and 5 keV) [12, 18]. This range includes elements such as phosphorus and sulfur which are of great interest in earth and environmental sciences, battery development, and catalysis research. These elements have a wide range of oxidation states, and can chemically bond with other elements and change the electrochemical structure of the materials of interest [10, 19, 20]. Thus, there is a great potential and interest in applications with high-resolution synchrotron-based XES measurement in the tender x-ray range. One of the main challenges associated with the low energy x-ray is the lack of the penetration through ambient environment, thus most of the tender x-ray XES systems thus far were used in vacuum and for bulk samples and are unsuitable for in-situ experiments [18, 21–24].

Recently, a state of art glovebox-integrated XES spectrometer (BRIMSTONE-GBX by easyXAFS LLC [25]) was commissioned at the soft x-ray microcharacterization beamline (SXRMB) at the canadian light source (CLS). SXRMB is a bending-magnet-based beamline that utilizes InSb(111) and Si(111) crystals for monochromatization to cover an energy range of 1.7–10 keV, with its main research focus in the tender energy (1.7–5 keV) [26, 27]. This unique energy range makes it possible to study important systems with both tender energy region elements (e.g. S, P, and Cl) as well as transition metals (e.g. Ni and Co), such as the lithium-ion batteries and sulfur related redox processes common in environmental research. Because of the compact design of the spectrometer, it is possible to fit the spectrometer into a helium gas filled and low moisture and oxygen content (below 1 ppm) glovebox, which not only makes the low energy x-ray penetration feasible but it can also be used for *in situ* and in operando studies. In addition, the endstation can be equipped with a Silicon Drift Detector (SDD) for XAS measurements in fluorescence yield mode. This paper reports the design, capabilities and performance of the glovebox-integrated XES spectrometer endstation at the SXRMB along with an example for *in situ* and in-operando measurements in battery development.

2. Glovebox-integrated XES spectrometer

Figure 1 shows the assembly of the glove box-integrated XES spectrometry station at SXRMB. The BRIMSTONE-GBX spectrometer operates in the dispersive refocusing Rowland (DRR) geometry, in which a focusing circle is defined by a crystal analyzer. A position-sensitive detector (kromo-TX1 x-ray camera by easyXAFS, LLC) is placed on the circle at the focusing position. Sample is placed inside the focusing circle and is illuminated by the incident beam. The key aspects of this geometry are: (1) the focusing circle is defined by the position of the analyzer and detector irrespective of the sample; (2) different emission energies are refocused onto different positions of the detector, since different positions correspond to different Bragg angles with the face of the crystal analyzer; (3) the bandwidth being captured is determined both by the width of the detector, and also by the width of the illuminated sample [28]. The spectrometer is mounted to X, Y, and Z linear stages for alignment with the incident beam. The spectrometer assembly consists of three main components: sample stage, crystal analyzer and position-sensitive detector. The rotary sample holder, which is placed on a sample wheel motor, can hold up to 15 samples at the same time. The crystal analyzer and position-sensitive detector are mounted on a mechanical system that allows the remote tuning of the Bragg angle and energy for the measurement of different emission lines and elements. The compact size of the spectrometer assembly is made possible by the small radius of curvature (10 cm) of the crystal analyzer, which sets the diameter of the Rowland circle at 10 cm. The entire assembly is then installed inside a specially designed glovebox with a port for the incoming x-ray beam. The glovebox is filled with helium gas to serve dual purpose; (1) acting as an inert atmosphere for the samples and (2) allowing for a helium beam path needed to reduce absorption of the tender x-ray beam. In addition, there is room inside the glovebox to house the components for in-situ experiments and an SDD so that XAS and XES measurements can be performed at the same time for a given sample. The plane of the spectrometer is rotated 10 degrees from perpendicular to the incident beam direction to reduce the intensity of elastic scatter but allow a small amount for calibration.

2.1. Capabilities

High energy resolution x-ray emission spectra are collected with the crystal analyzer and position-sensitive detector at a fixed position for a specific emission line, while keeping the incident beam energy constant. The spectrum is obtained by processing the measured 2D image and calculating the energy spectrum based on the 10 cm Rowland geometry, and the energies of reference samples or the elastic peak of the incoming x-ray. If the incident energy is far above the x-ray absorption edge of the element of interest, then non-resonant x-ray emission spectra can be recorded. The incident photon energy could be tuned below or close to the absorption edge, in order to collect the resonant x-ray emission spectra. Moreover, by scanning the incident energy across the absorption edge of the element of interest, resonant inelastic x-ray scattering (RIXS) and consequently high energy resolution fluorescence detection (HERFD) measurements can be performed as well.

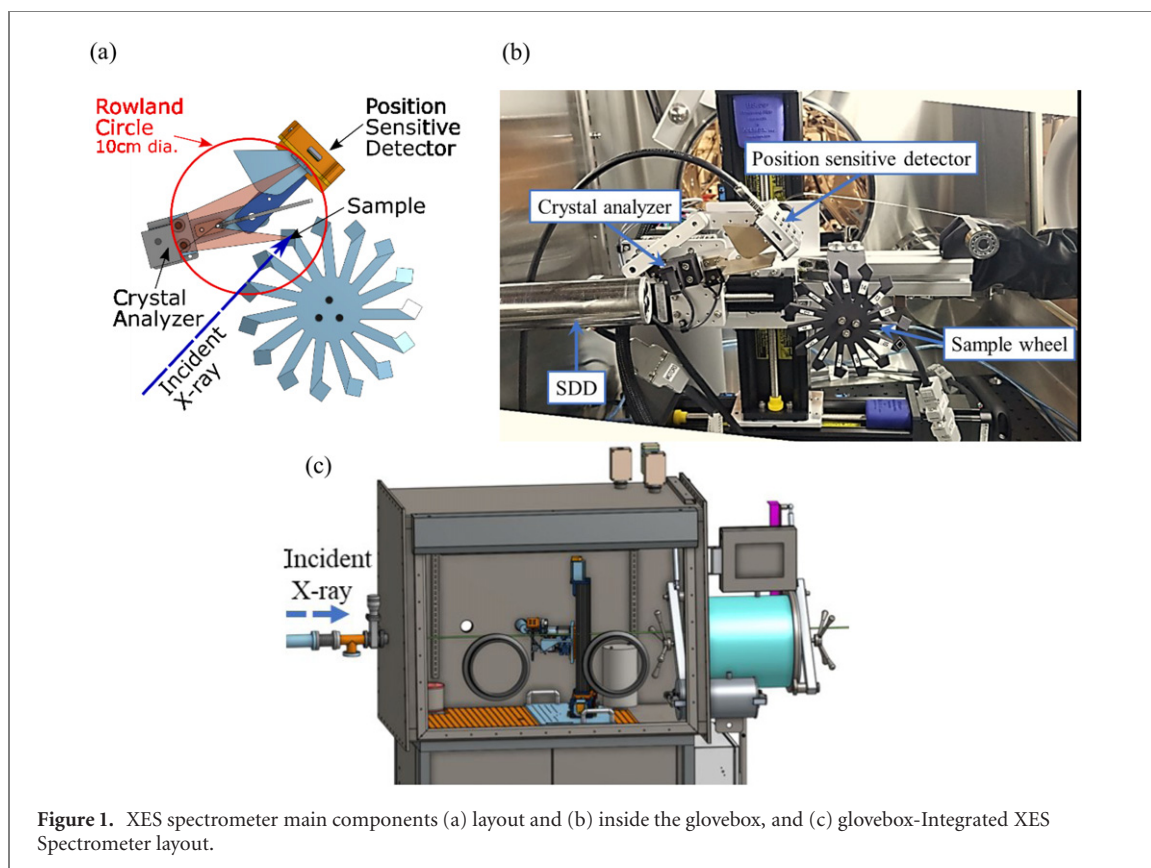


Figure 1. XES spectrometer main components (a) layout and (b) inside the glovebox, and (c) glovebox-Integrated XES Spectrometer layout.

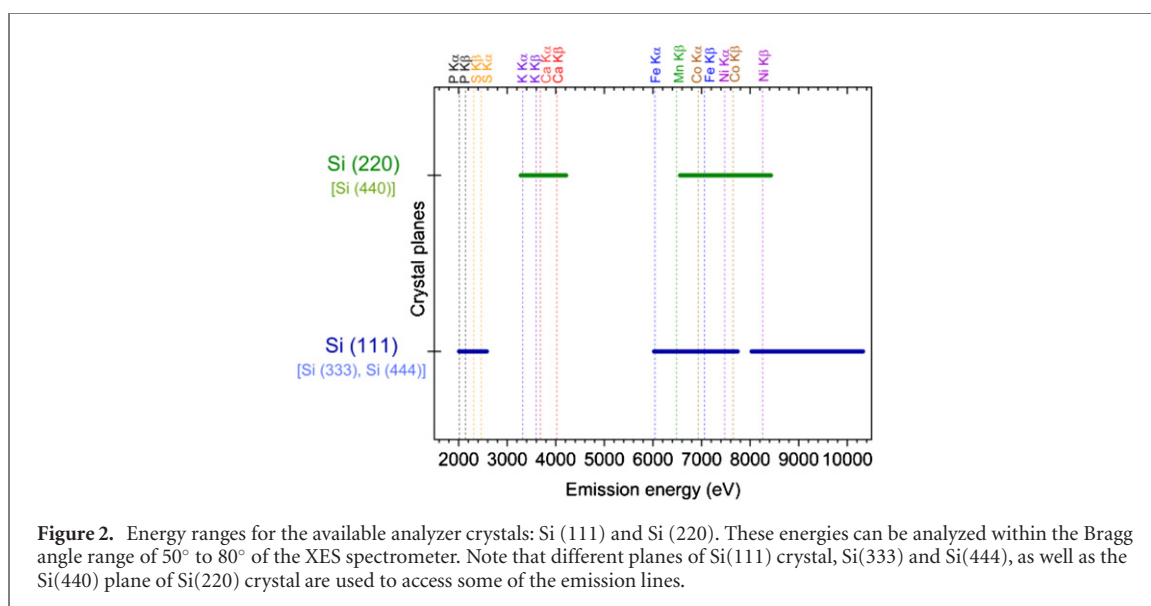
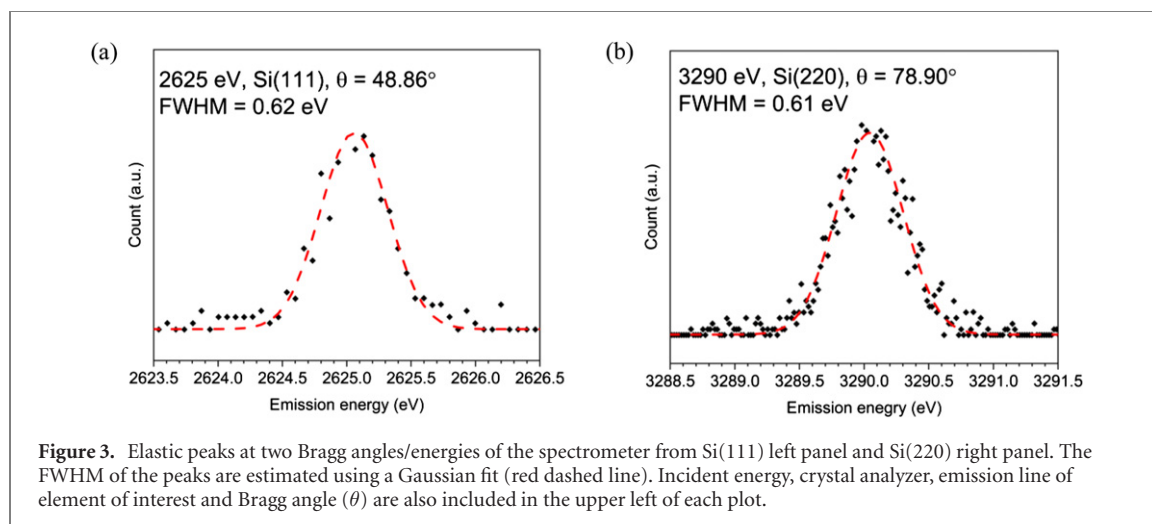


Figure 2. Energy ranges for the available analyzer crystals: Si (111) and Si (220). These energies can be analyzed within the Bragg angle range of 50° to 80° of the XES spectrometer. Note that different planes of Si(111) crystal, Si(333) and Si(444), as well as the Si(440) plane of Si(220) crystal are used to access some of the emission lines.

Considering the beamline energy range of the SXRMB (1.7–10 keV), Bragg angle range (50° – 80°) of the XES spectrometer, the choice of available Si(111) and Si(220) cylindrically bent crystals as well as their matching parallel planes [Si(333), Si(444) and Si(440)], and Bragg's Law, the energy range that can be captured with the XES spectrometer are calculated and shown in figure 2. As examples shown in figure 2, our XES spectrometer station is capable of measuring $K\alpha$ and $K\beta$ emission lines of tender x-rays from elements such as S and P as well as first row transition metals.

2.2. Spectrometer control and data acquisition

Dedicated software written in Python/Epics programming environment running under Linux is developed to control the stepper motors controlling the mechanical parts of the spectrometer. A graphical user interface (GUI) is also developed to connect the beamline master computer to the spectrometer computer. The raw



2D-images are collected by the position-sensitive detector. A Python based program is used to process the 2D-images to obtain the final spectra (intensity vs energy scale) in an ASCII format. The shape of the signal of the 2D-images is curved because of the use of a cylindrically shaped crystal analyzer. The Python program uses a second-order polynomial fit to this curvature to assign each pixel to a curved bin. After the signal is processed, a one-point energy calibration is applied using a known energy position to assign the angle of a curved bin, and then using geometrical calculations based on the known Rowland geometry to assign angles for the other bins. When higher calibration accuracy is necessary, additional calibration points can be used to correct the energy scale.

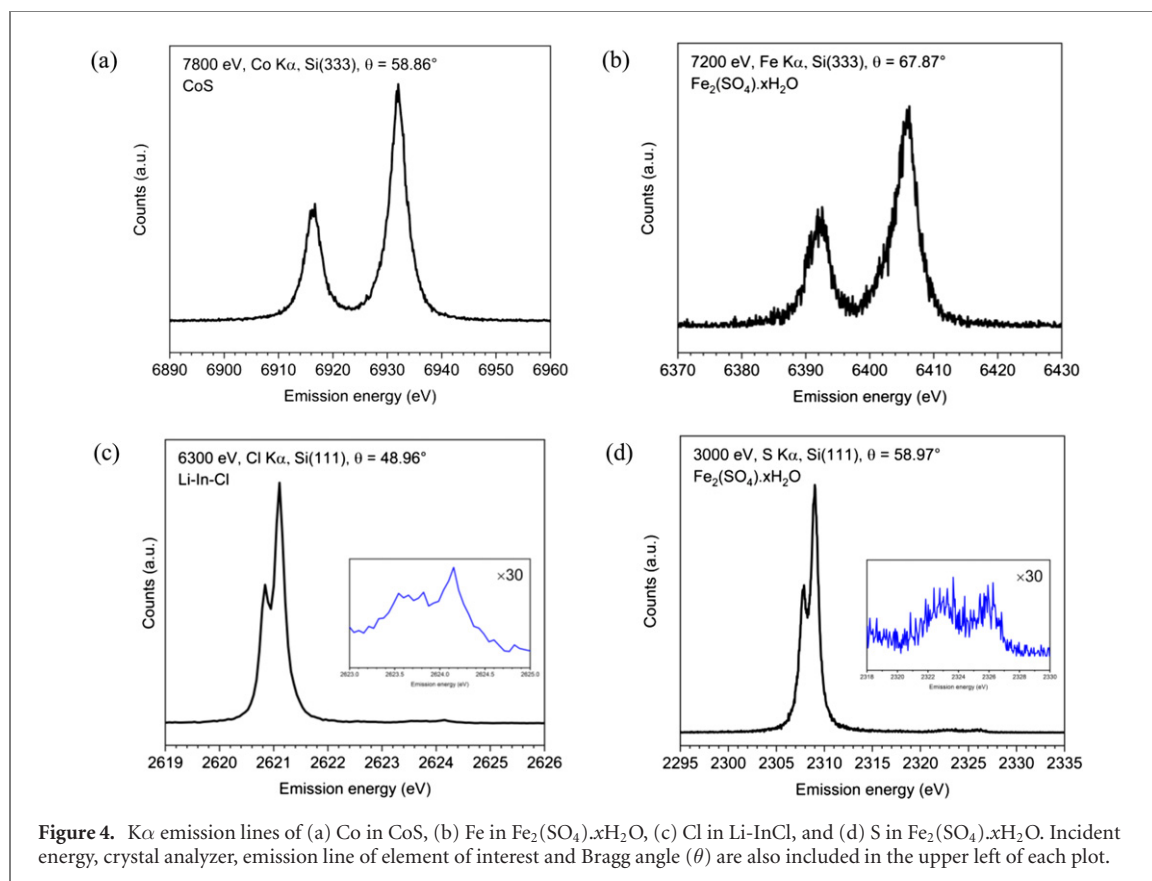
2.3. Energy calibration and resolution

A typical procedure for energy calibration is to collect the XES spectra of the desired emission line using a standard/reference sample. Since the emission lines of a reference are known, their spectra can be used to calibrate the pixels of the raw image to their corresponding energy of the collected standard spectra and thereby calibrate the energy scale for the rest of the samples. Another method, by relying on energy calibration of the incident x-rays, is to use the elastic peak at different incident energies. Though very weak, a small portion of the incident beam from the beamline is elastically scattered, thus allowing the XES energy scale to be calibrated against the beamline monochromator. Then the energy scale could be calibrated without use of any standard/reference materials. It should be noted that incident energy of the beamline monochromator is calibrated by the XAS spectrum of a reference in the energy range of interest using the available SDD detector.

To estimate the energy resolution of the spectrometer, a series of tests were carried out to obtain elastic peaks at various incident energies. The incident beam was produced from either the Si(111) or InSb(111) crystal of the SXRMB depending on the element and its emission line; and Si(111) or Si(220) was chosen as the crystal analyzer for XES measurements. The spectra thus collected were then fitted using a Gaussian function to calculate the full width at half maximum (FWHM) of the peaks. Knowing the FWHM of the collected peaks as well as FWHM of mono ($\text{FWHM}_{\text{mono}}$), FWHM of the spectrometer ($\text{FWHM}_{\text{spec}}$) can be estimated using a quadrature, $\text{FWHM}_{\text{spec}} = \sqrt{\text{FWHM}^2 - \text{FWHM}_{\text{mono}}^2}$ [16]. Figure 3 shows two examples of the collected spectra of scattered signals at different geometries and the calculated FWHMs for different energy regions. From the FWHM values shown in figure 3, it is clear that the energy resolution of the spectrometer is always better than 1 eV (~ 0.6 eV) in the tender x-ray energy range of 2.6 to 3.3 keV. It is noteworthy that this high resolution is necessary to distinguish between the $\text{K}\alpha_1$ and $\text{K}\alpha_2$ emission lines of the lightest elements in SXRMB energy range. For example, $\text{K}\alpha_1$ and $\text{K}\alpha_2$ lines of phosphorus are at 2013.7 eV and 2012.7 eV and for sulfur are at 2307.8 eV and 2306.6 eV, respectively. While for heavier elements, the difference between the lines is greater than few electron volts (i.e. Fe $\text{K}\alpha_1$ and $\text{K}\alpha_2$ are at 6403.8 eV and 6390.8 eV, respectively). Also, such elastic scattering signals (figure 3) can be later used to calibrate the pixels of the position-sensitive detector and consequently the collected spectra for the line of interest.

2.4. Examples of collected $\text{K}\alpha$ and $\text{K}\beta$ emission lines

Figure 4 shows several examples of $\text{K}\alpha$ lines collected from main group elements in the energy range of tender x-ray as well as transition metals. In all cases, core-to-core $\text{K}\alpha_1$ ($2p_{3/2} \rightarrow 1s$) and $\text{K}\alpha_2$ ($2p_{1/2} \rightarrow 1s$) are clearly resolved. These spectra demonstrate a wide energy range and resolution of our spectrometer, designed to probe the chemical structure of both main group elements (S, P, and Cl) and transition metals. For example, non-resonant XES of S $\text{K}\alpha$ in iron sulfate hydrate, shows $\text{K}\alpha_1$ and $\text{K}\alpha_2$ at ~ 2307.8 eV and ~ 2309 eV, respectively.

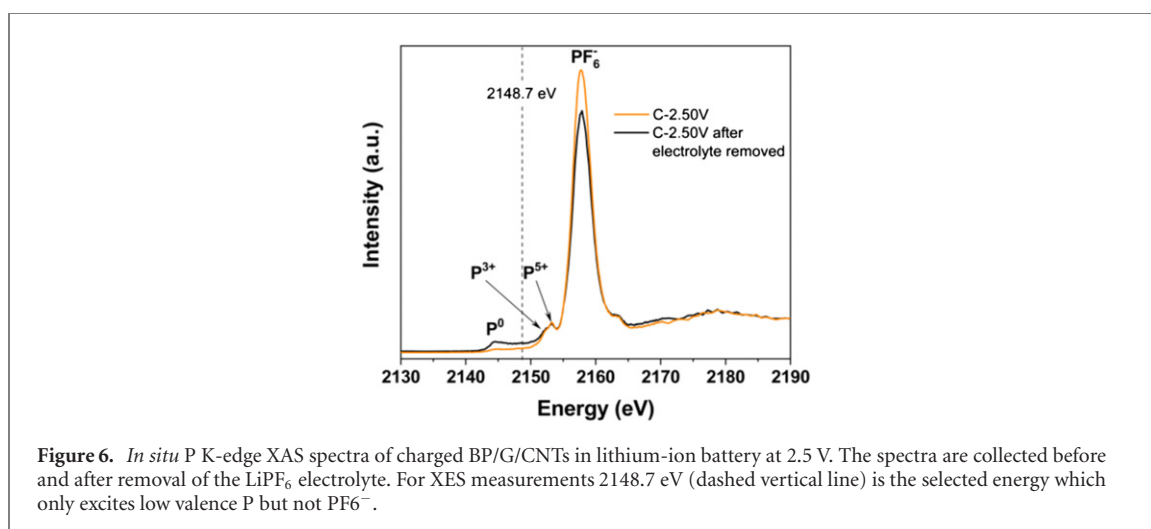
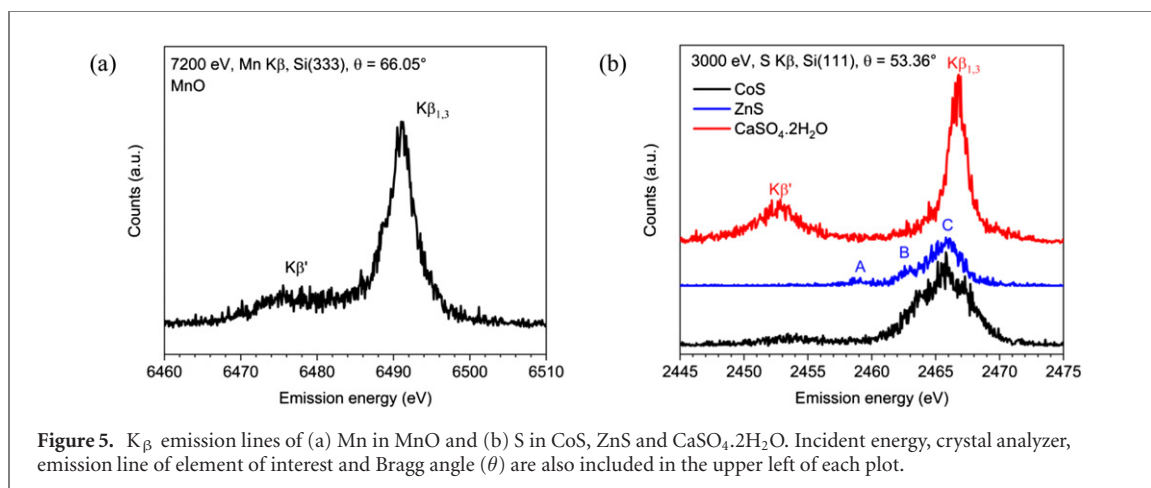


A closer look at the spectra even reveals the satellite peaks (as shown in the insert) from many-body effects because of the non-resonant incident energy (3000 eV) [29, 30].

In addition to the $K\alpha$ lines, figure 5 shows the Mn and S $K\beta$ x-ray emission valence-to-core spectra as examples of transition metal and main group intermediate Z elements, respectively. In the case of Mn $K\beta$, there are two peaks identified at 6474.5 eV and 6490.1 eV corresponding to $K_{\beta_{1,3}}$ and $K_{\beta'}$ lines of Mn^{2+} , respectively [31]. For sulfur, $K\beta$ emission line (from 3p or higher levels \rightarrow 1s), compared to the $K\alpha$, probes the valence to core electron emission; thus, $K\beta$ can provide more directly chemical information about the ligands and their type in a chemical structure. In case of the collected sulfur spectra, the origin of the $K_{\beta'}$ feature is different for different compounds and in the case of sulfate it is due to orbital hybridization with the oxygen 2p orbitals. Figure 5 clearly shows the chemical sensitivity of collected S $K\beta$ lines to differentiate sulfate from sulfide samples. The larger splitting of the $K_{\beta_{1,3}}$ and $K_{\beta'}$ features in the $\text{CaSO}_4\cdot 2\text{H}_2\text{O}$ spectrum reveals larger number of unpaired S electrons in oxidized sulfur (S^{6+}) than in reduced sulfur (S^{2-}) [19]. Figure 5 also reveals that S $K\beta$ lines are also sensitive to different sulfides. For the ZnS sample, there are three main features: a prominent peak, C; a shoulder at lower energy, B; and a peak at lower energy than B, A. While there are two peaks (B and C) around 2465 eV for CoS, the presence of a peak near 2453 eV in the CoS sample suggests the presence of sulfate due to the surface oxidation of the sample. Alonso Mori *et al* surveyed a wide variety of sulfide compounds and found no spectral features lower than 2459 eV in energy, while sulfur–oxygen compounds (SO_x) all show prominent $K_{\beta'}$ peaks in this energy range, as in the case of $\text{CaSO}_4\cdot 2\text{H}_2\text{O}$ (figure 5(b)) [19]. This oxidized sulfur species on CoS was confirmed by a separate $K\alpha$ XES measurement. These examples further demonstrate the capability of SXRMB XES to probe the ligands and can be used as a complementary tool to other characterization techniques to better understand the chemical structure of the element of interest.

3. Application in battery research

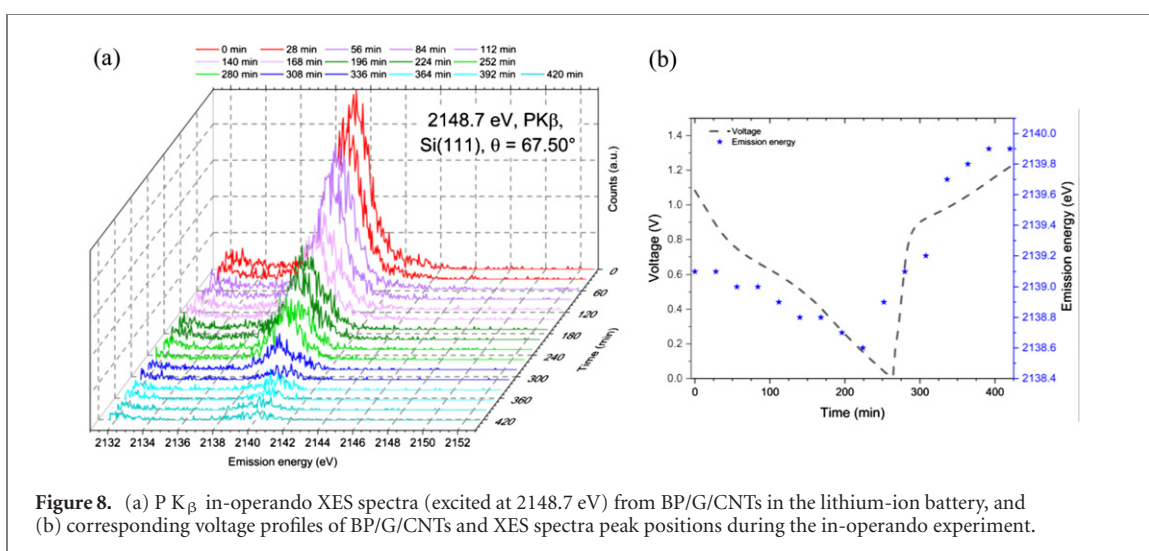
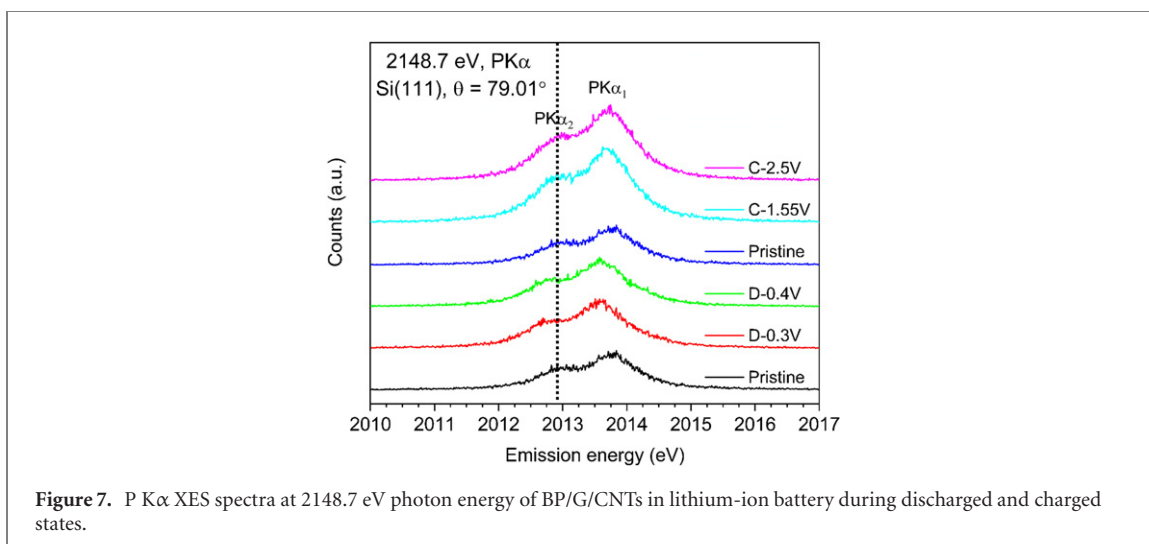
Lithium-ion batteries (LIBs) have been extensively used in portable devices such as laptops, cellphones and electrical vehicles since the 2000s [32, 33]. Materials such as LiCoO_2 , LiFePO_4 and LiMn_2O_4 are commonly used as cathode in LIBs [34]. Phosphorus, because of its higher theoretical capacity (2592 mA h g^{-1}), has been known as a promising anode material in the LIBs [35]. White phosphorus (WP), black phosphorus (BP) and red phosphorus (RP) are the three phosphorus allotropes. WP is chemically unstable and ignites in air, thus it is not a safe choice to be used in LIBs. BP is thermodynamically stable and has higher carrier mobility and



electrical conductivity than RP. Thus, BP can be a promising candidate as an anode material for LIBs [36, 37]. To obtain/develop a stable battery, understanding the phase transformation of phosphorus (i.e. P, LiP, Li_3P , Li_3P_7) in LIBs during charge and discharge cycles is crucial [38–40].

X-ray based characterization techniques such as XRD, XAS and XES can be used to probe the phosphorus chemical changes of a nanostructured black phosphorus–graphite–single–walled carbon nanotube (BP/G/CNTs) composite during charge and discharge cycles in LIBs. XRD is only sensitive to the crystalline samples, while some of the Li–P intermediates (i.e. Li_3P_7 , LiP) can be in amorphous phases and thus cannot be detected with XRD [35, 40]. To understand the chemical changes in LIBs, XAS of P K-edge is necessary to track the ionic process, while metal K-edge (such as Fe K-edge in the case of LiFePO_4) is used to understand the electron transportation in such batteries. In SXRMB we can study the XAS of both P and Fe K-edge [41]. However, the *in-situ* XAS at the P K-edge of BP based LIB can be challenging due to the interference of the P-containing electrolyte (LiPF_6). As shown in figure 6, the *in situ* XAS P K-edges spectrum was dominated by the PF_6^- signal around 2158 eV, due to the strong contribution of the electrolyte. It is difficult to study the change in the state of BP anode, even after removal of the electrolyte upon the charging of the LIB (figure 6). By selecting the photon energy so that the phosphorus in LiPF_6 is not excited but BP which has a lower threshold remains excited, x-ray emission spectroscopy can overcome this problem. We should also note that it takes about 10 mins to collect a proper near edge XAS at P K-edge, while a full XES spectrum takes about 1 min at each charged/discharged state. Thus, XES is more suitable for the *in-situ* measurements of LIBs under high charge rate and for kinetic studies.

Figure 7 shows the P $K\alpha$ *in situ* XES spectra from the BP/G/CNTs assembly in the battery at different stages of discharge (D–) and charge (C–). The incident x-ray energy for the XES measurements was set at 2148.7 eV (figure 6), which is above the threshold of the low oxidation states of P, but below the absorption threshold of P(III), P(V) and PF_6^- (figure 6). Thus, the contribution of high P oxidation states and the electrolyte can be



excluded. The XES spectra of all samples clearly show two separate peaks with intensity ratio of about 2 to 1 (figure 7). These peaks are attributed to the P K α_1 (~ 2013.80 eV) and P K α_2 (~ 2012.92 eV) fluorescence lines, respectively, resulting from the decay of electrons in phosphorus atom from $2p_{1/2}$ and $2p_{3/2}$ states to $1s$ core hole. It is clear that the XES peaks generally shift to lower energy during discharge, gaining electrons (BP \rightarrow Li $_3$ P) and to higher energy during charge, losing electrons (Li $_3$ P \rightarrow BP). Also, the pristine and C-2.50V (charged battery at 2.5 V) states have similar PK α_1 and PK α_2 positions at 2012.93 eV and 2013.75 eV, respectively. By combining the XAS, XES and XRD results, it was found that BP undergoes step-by-step phase transformation to Li $_3$ P $_7$, LiP and Li $_3$ P, and transfers back gradually during charging (Li M *et al*, to be published). This indicates that the lithiation / delithiation process of BP nanoparticles is fully reversible during the initial cycle.

In addition to the use of K α lines, it is also possible to study the transformation of phosphorus using P K β lines during the operation of the BP/G/CNTs based LIB, as K β lines are weaker, but more chemically sensitive than the K α lines. Figure 8(a) shows a full set of P K β XES spectra with the photon energy set at 2148.7 eV and each spectrum is collected for 4 min. Similar to P K α , the main peak shifts to lower energies with the decreasing voltage (~ 2139.1 eV at 1.2 V at time 0 to ~ 2138.6 eV at ~ 0.2 eV & 224 min) and to higher energies when the voltage is increasing, as shown in figure 8(b) (from ~ 2138.6 eV at ~ 0.2 eV & 224 min to ~ 2139.9 eV at 1.4 V & 420 min). These energy shifts correspond to the change in the state of phosphorus during the cycle from Li $_3$ P (and/or other Li–P intermediates) to BP and further confirm the reversible lithiation / delithiation process of BP nanoparticles. We should note that the XES spectra became weaker and noisier as a function of the time, which is caused by the surface accumulation of electrolyte. This case demonstrates that the glovebox-integrated XES spectrometer can be used for in-operando experiments to obtain complementary information that can be extracted for the occupied states. This shows the feasibility of such apparatus to battery research studies especially in tender x-ray energy region elements such as phosphorus and sulfur.

4. Conclusions

The glovebox-integrated Rowland-type XES spectrometer has recently been installed and is now operational at SXRMB beamline (1.7–10 keV) at the CLS. The endstation is also equipped with an SDD to collect XAS spectra. The spectrometer, which is installed in a helium filled glovebox, consists of a choice of two crystal analyzers (Si(111) and Si(220)) as well as their matching parallel planes [Si(333), Si(444) and Si(440)], a position-sensitive detector, and a sample wheel which can accommodate multiple samples at the same time. This unique energy range and excellent resolution of the beamline as well as the helium environment, makes this setup capable of studying both tender-energy region main group elements (i.e. S, P, Cl, etc) as well as first row transition metals (i.e. Ni, Co, etc). The *in situ* and in-operando XES measurements over lithium-ion battery has clearly demonstrated the wide range applicability of the glovebox-integrated XES station in materials studies.

Acknowledgments

The XES instrument was funded by an NSERC RTI grant (Western) and a matching equipment grant from the Canadian Light Source. This work was performed at the Canadian Light Source, a national research facility at the University of Saskatchewan, which is supported by the Canada Foundation for Innovation (CFI), the Natural Sciences and Engineering Research Council (NSERC), the National Research Council (NRC), the Canadian Institutes of Health Research (CIHR), the Government of Saskatchewan, and the University of Saskatchewan. Research at Western was supported by NSERC, CRC, CFI and ORF. Technical support from CLS staff is gratefully acknowledged.

ORCID iDs

Mohsen Shakouri  <https://orcid.org/0000-0002-8449-9763>

References

- [1] Brock J D and Sutton M 2008 Materials science and x-ray techniques *Mater. Today* **11** 52–5
- [2] Lombi E and Susini J 2009 Synchrotron-based techniques for plant and soil science: opportunities, challenges and future perspectives *Plant Soil* **320** 1–35
- [3] Gallo E and Glatzel P 2014 Valence to core x-ray emission spectroscopy *Adv. Mater.* **26** 7730–46
- [4] van Bokhoven J A and Lamberti C 2015 *X-Ray Absorption and X-Ray Emission Spectroscopy: Theory and Applications* vol 1–2 ed J A Van Bokhoven and C Lamberti (Chichester: Wiley Ltd)
- [5] Lin F *et al* 2017 Synchrotron x-ray analytical techniques for studying materials electrochemistry in rechargeable batteries *Chem. Rev.* **117** 13123–86
- [6] Chen F, Hu J, Takahashi Y, Yamada M, Rahman M S and Yang G 2019 Application of synchrotron radiation and other techniques in analysis of radioactive microparticles emitted from the Fukushima Daiichi nuclear power plant accident—a review *J. Environ. Radioact.* **196** 29–39
- [7] Weckhuysen B M 2005 *In situ* spectroscopy of catalysts *ChemInform* **36**
- [8] Weckhuysen B M 2010 Preface: recent advances in the *in situ* characterization of heterogeneous catalysts *Chem. Soc. Rev.* **39** 4557–9
- [9] Li X, Yang X, Zhang J, Huang Y and Liu B 2019 *In situ/operando* techniques for characterization of single-atom catalysts *ACS Catal.* **9** 2521–31
- [10] Alonso Mori R, Paris E, Giuli G, Eeckhout S G, Kavčič M, Žitnik M, Bučar K, Pettersson L G M and Glatzel P 2009 Electronic structure of sulfur studied by x-ray absorption and emission spectroscopy *Anal. Chem.* **81** 6516–25
- [11] Kleymenov E *et al* 2011 Five-element Johann-type x-ray emission spectrometer with a single-photon-counting pixel detector *Rev. Sci. Instrum.* **82** 065107
- [12] Kavčič M, Budnar M, Mühleisen A, Gasser F, Žitnik M, Bučar K and Bohinc R 2012 Design and performance of a versatile curved-crystal spectrometer for high-resolution spectroscopy in the tender x-ray range *Rev. Sci. Instrum.* **83** 033113
- [13] Llorens I *et al* 2012 High energy resolution five-crystal spectrometer for high quality fluorescence and absorption measurements on an x-ray absorption spectroscopy beamline *Rev. Sci. Instrum.* **83** 063104
- [14] Kvashnina K O and Scheinost A C 2016 A Johann-type x-ray emission spectrometer at the Rossendorf beamline *J. Synchrotron Radiat.* **23** 836–41
- [15] Sokaras D *et al* 2013 A seven-crystal Johann-type hard x-ray spectrometer at the stanford synchrotron radiation lightsource *Rev. Sci. Instrum.* **84** 053102
- [16] Nowak S H *et al* 2020 A versatile Johansson-type tender x-ray emission spectrometer *Rev. Sci. Instrum.* **91** 033101
- [17] Kalinko A, Caliebe W A, Schoch R and Bauer M 2020 A von Hamos-type hard x-ray spectrometer at the PETRA III beamline P64 *Kalinko Aleksandr J. Synchrotron Radiat.* **27** 31–6
- [18] Northrup P, Leri A and Tappero R 2016 Applications of ‘tender’ energy (1–5 keV) x-ray absorption spectroscopy in life sciences *Protein Pept. Lett.* **23** 300–8
- [19] Alonso Mori R, Paris E, Giuli G, Eeckhout S G, Kavčič M, Žitnik M, Bučar K, Pettersson L G M and Glatzel P 2010 Sulfur-metal orbital hybridization in sulfur-bearing compounds studied by x-ray emission spectroscopy *Inorg. Chem.* **49** 6468–73
- [20] Petric M, Bohinc R, Bučar K, Žitnik M, Szlachetko J and Kavčič M 2015 Chemical state analysis of phosphorus performed by x-ray emission spectroscopy *Anal. Chem.* **87** 5632–9

- [21] Morel F L, Pin S, Huthwelker T, Ranocchiari M and Van Bokhoven J A 2015 Phosphine and phosphine oxide groups in metal-organic frameworks detected by P K-edge XAS *Phys. Chem. Chem. Phys.* **17** 3326–31
- [22] Gu C, Dam T, Hart S C, Turner B L, Chadwick O A, Berhe A A, Hu Y and Zhu M 2020 Quantifying uncertainties in sequential chemical extraction of soil phosphorus using XANES spectroscopy *Environ. Sci. Technol.* **54** 2257–67
- [23] Li W et al 2020 Phosphorene degradation: visualization and quantification of nanoscale phase evolution by scanning transmission x-ray microscopy *Chem. Mater.* **32** 1272–80
- [24] Acksel A, Baumann K, Hu Y and Leinweber P 2019 A critical review and evaluation of some P-research methods *Commun. Soil Sci. Plant Anal.* **50** 2804–24
- [25] Holden W M 2020 EasyXAFS BRIMSTONE tender spectrometer <http://easyxafs.com/instruments/#tender-xray>
- [26] Hu Y F et al 2010 Preliminary commissioning and performance of the soft x-ray micro-characterization beamline at the Canadian light source *AIP Conf. Proc.* **1234** 343–6
- [27] Xiao Q, MacLennan A, Hu Y, Hackett M, Leinweber P and Sham T K 2017 Medium-energy microprobe station at the SXRMB of the CLS *J. Synchrotron Radiat.* **24** 333–7
- [28] Holden W M et al 2017 A compact dispersive refocusing Rowland circle x-ray emission spectrometer for laboratory, synchrotron, and XFEL applications *Rev. Sci. Instrum.* **88** 073904
- [29] Yasuda S and Kakiyama H 1979 Chemical effects in x-ray $K\alpha$ and $K\beta$ emission spectra of sulfur in organic compounds *Spectrochim. Acta Part A Mol. Spectrosc.* **35** 485–93
- [30] Ouyang J F and Bettens R P A 2016 When are many-body effects significant? *J. Chem. Theory Comput.* **12** 5860–7
- [31] Glatzel P, Smolentsev G and Bunker G 2009 The electronic structure in 3d transition metal complexes: can we measure oxidation states? *J. Phys. Conf. Ser.* **190** 012046
- [32] Bruce P G, Scrosati B and Tarascon J M 2008 Nanomaterials for rechargeable lithium batteries *Angew. Chemie - Int. Ed.* **47** 2930–46
- [33] Li M, Lu J, Chen Z and Amine K 2018 30 Years of lithium-ion batteries *Adv. Mater.* **30** 1800561
- [34] Kim Y, Park Y, Choi A, Choi N S, Kim J, Lee J, Ryu J H, Oh S M and Lee K T 2013 An amorphous red phosphorus/carbon composite as a promising anode material for sodium ion batteries *Adv. Mater.* **25** 3045–9
- [35] Mayo M, Griffith K J, Pickard C J and Morris A J 2016 *Ab initio* study of phosphorus anodes for lithium- and sodium-ion batteries *Chem. Mater.* **28** 2011–21
- [36] Hembram K P S S, Jung H, Yeo B C, Pai S J, Kim S, Lee K R and Han S S 2015 Unraveling the atomistic sodiation mechanism of black phosphorus for sodium ion batteries by first-principles calculations *J. Phys. Chem C* **119** 15041–6
- [37] Yasaei P, Kumar B, Foroozan T, Wang C, Asadi M, Tuschel D, Indacochea J E, Klie R F and Salehi-Khojin A 2015 High-quality black phosphorus atomic layers by liquid-phase exfoliation *Adv. Mater.* **27** 1887–92
- [38] Sun L Q, Li M J, Sun K, Yu S H, Wang R S and Xie H M 2012 Electrochemical activity of black phosphorus as an anode material for lithium-ion batteries *J. Phys. Chem C* **116** 14772–9
- [39] Park C M and Sohn H J 2007 Black phosphorus and its composite for lithium rechargeable batteries *Adv. Mater.* **19** 2465–8
- [40] Jung S C and Han Y K 2015 Thermodynamic and kinetic origins of lithiation-induced amorphous-to-crystalline phase transition of phosphorus *J. Phys. Chem C* **119** 12130–7
- [41] Wang D, Wang H, Yang J, Zhou J, Hu Y, Xiao Q, Fang H and Sham T-K 2016 Dynamic study of sub-micro sized LiFePO₄ cathodes by in-situ tender x-ray absorption near edge structure *J. Power Sources* **302** 223–32